

Article

Not peer-reviewed version

# Application of diceCT to Study the Development of the Zika Virus Infected Mouse Brain

[Amy L Green](#) , [Evangeline C Cowell](#) , [Laura M Carr](#) , [Kim Hemsley](#) , Emma Sherratt , [Lyndsey Collins-Praino](#) , [Jillian M Carr](#) \*

Posted Date: 10 July 2024

doi: 10.20944/preprints202407.0791.v1

Keywords: CT; brain imaging; congenital zika syndrome



Preprints.org is a free multidiscipline platform providing preprint service that is dedicated to making early versions of research outputs permanently available and citable. Preprints posted at Preprints.org appear in Web of Science, Crossref, Google Scholar, Scilit, Europe PMC.

Copyright: This is an open access article distributed under the Creative Commons Attribution License which permits unrestricted use, distribution, and reproduction in any medium, provided the original work is properly cited.

## Article

# Application of diceCT to Study the Development of the Zika Virus Infected Mouse Brain

**Running title:** the use of diceCT for imaging the ZIKV-infected mouse brain

Amy L Green <sup>1,2</sup>, Evangeline C Cowell <sup>1,2</sup>, Laura M Carr <sup>3</sup>, Kim Hemsley <sup>1,2</sup>, Emma Sherratt <sup>4</sup>,  
Lyndsey Collins-Praino <sup>3</sup> and Jillian M Carr <sup>1,2,\*</sup>

<sup>1</sup> College of Medicine and Public Health, Flinders University, GPO Box 2100, Adelaide, SA, 5001, Australia

<sup>2</sup> Flinders Health and Medical Research Institute, Flinders University, Adelaide, South Australia, Australia

<sup>3</sup> School of Biomedicine, The University of Adelaide, Adelaide, South Australia 5005, Australia

<sup>4</sup> School of Biological Sciences, The University of Adelaide, Adelaide, South Australia 5005, Australia

\* Correspondence: ill.carr@flinders.edu.au

**Abstract:** Zika virus (ZIKV) impacts the developing brain. Here a technique was applied to define, in 3D, developmental changes in the brain of ZIKV-infected mice. Postnatal day 1 mice were uninfected or ZIKV-infected, then analysed by iodine staining and micro-CT scanning (diffusible iodine contrast enhanced micro-CT; diceCT) at 3-, 6- and 10-days post infection (dpi). Multiple brain regions were visualised using diceCT; olfactory bulb, cerebrum, hippocampus, midbrain, interbrain, and cerebellum, along with the lens and retina of the eye. Brain regions were computationally segmented and quantitated, with increased brain volumes with developmental time in uninfected mice. Conversely, in ZIKV-infected mice, no quantitative differences were seen at 3 or 6 dpi, when there are no clinical signs, but qualitatively, diverse visual defects were identified at 6-10 dpi. By 10 dpi, ZIKV-infected mice had significantly lower body weight and reduced volume of brain regions compared to 10 dpi-uninfected or 6dpi ZIKV-infected mice. Nissl and immunofluorescent Iba1 staining on post-diceCT tissue were successful, but RNA extraction was not. Thus, diceCT shows utility for detecting both 3D qualitative and quantitative changes in the developing brain of ZIKV-infected mice, with the benefit, post-diceCT, of retaining the ability to apply traditional histology and immunofluorescent analysis to tissue.

**Keywords:**

## Introduction

Zika virus (ZIKV) is a positive-sense single-stranded RNA virus in the *flavivirus* genus, where clinically significant outbreaks culminated in the 2016 World Health Organisation (WHO) declaration of a Public Health Emergency of International Concern [1,2]. Vertical transmission of ZIKV from mother to child *in utero* is the primary clinical concern, with adverse consequences in the developing fetus [3–5]. The neurological and developmental effects of fetal ZIKV infection is termed congenital zika syndrome (CZS) [6]. The most common and identifiable pathology in human neonates is microcephaly, defined clinically as a reduction in head circumference [6–8], although neurological deficits are also observed in the absence of microcephaly [5,9–13]. Radiological findings, such as by magnetic resonance imaging (MRI) or X-ray computed tomography (CT) scanning of the brain of ZIKV-affected babies, show some common abnormalities, such as calcifications in various regions of the brain [11,14–16], ventriculomegaly and reduced gyrification (ie a reduction in the folding of the surface of the brain) [17]. In addition, less common brain pathologies include cerebellar hypoplasia or dysplasia, periventricular septation and hydrocephalus, highlighting the diversity of CZS [18]. There is also ocular involvement, with findings such as retinal scarring and mottling [6,19,20]. Some of the diversity observed between CZS cases may relate to the timing of ZIKV infection during pregnancy [5,21].

The molecular basis for CZS has been informed from many studies demonstrating ZIKV-infection and cell killing of neural progenitor cells *in vitro* and *in vivo* [22–25]. Studies also suggest that, in addition to neurons, astrocytes and microglia are susceptible to infection and viral induction of cell death and contribute to ZIKV-induced brain pathology [22,26,27]. Additionally, mouse models of ZIKV infection during pregnancy demonstrate dramatic effects on the brain, such as reduction in overall size, but often utilise immunodeficient mice, such as those lacking the interferon response, with subsequent severe brain impact and fetal demise [28]. This may reflect aspects of ZIKV-infection *in utero* associated with fetal loss in humans, but, importantly, many babies that are exposed to ZIKV *in utero* ultimately survive, with varying degrees of impairment at birth and evolving neurological impact [9,15]. Immunocompetent mouse models of direct brain infection of the embryo are established and also demonstrate impact on the brain, measured by both 2D image analysis and histology, such as areas of necrosis and cellular infiltrates in the cortex, hippocampus, thalamus and cerebellum at 21 days postnatally [25]. Immunocompetent mouse models of early postnatal (P1-P3) ZIKV infection result in acute ZIKV replication and inflammation 3-6 days post infection (dpi) [29] and demonstrate infection of the retina [30], as well as diverse cell types and regions of the brain. This includes astrocytes and neurons, with infection of the hippocampus and cerebral cortex, with the highest infected cell numbers in the cortex [31]. There are subsequent morphological changes in the brain that are consistent with the pathology in humans, including calcifications and ventriculomegaly [22,32–34]. These changes have been characterised both histologically and by MRI late in the course of disease in mice, (eg. 21- 30 dpi and into adulthood), and can be associated with on-going inflammation, cell death and reduced volume of the total brain assessed dorsally by gross morphology [22,35]. Our laboratory has used a similar post-natal ZIKV-infection model in immunocompetent mice [29] and tested the applicability of a relatively new research tool, diffusible iodine-based contrast-enhanced computed tomography (diceCT), to undertake a three dimensional (3D) *in situ* analysis of the early (3-10 day) morphology of the ZIKV-infected mouse brain during development and prior to the onset of overt disease. This time period in development reflects late *in utero* development of the brain and eye in humans and a period of rapid growth of the rodent brain [36,37].

DiceCT refers to the process of enhancing contrast of the soft tissue of a specimen via application of an iodine-based solution prior to CT scanning [38,39]. The use of micro-CT scanning provides high resolution and the visualisation of bone in small laboratory animals, while the iodine staining provides the contrast of soft tissue. The diceCT technique currently has major relevance in general morphological studies, for example in comparative anatomy and evolutionary studies [40,41], and in the digital preservation of museum specimens [42,43]. Additionally, diceCT has proven useful in recent biomedical and clinical applications, in order to study anatomical features [44,45], including brain tissue from laboratory animal and human specimens [46,47], but has not yet been applied to study viral pathology. In contrast, MRI is a widely used clinical imaging technique and useful to apply to living animals, although the machines are less available in the laboratory setting, due to costs and expertise required [48], and provide less resolution of the brain structures in small laboratory animals. While MRI has been combined with improved tissue contrasting using Mn ions (MEMRI) and applied to the P1-P11 developing mouse brain with excellent resolution and quantitative analysis [49], this still does not overcome the challenges of using MRI in most laboratory settings. diceCT is thus an alternative technique, with microCT scanning generally more available in core imaging facilities, and with outputs that allow for the acquisition of high-contrast soft tissue scans and 3D visualisation and analysis of these anatomical structures *in situ* within the natural restriction of bone. Further, post-diceCT stained tissue has the potential to be utilised for further downstream analysis, such as general histology, as benefits the research setting.

Here, application of diceCT to the early postnatal mouse, successfully discriminated regions of the brain, the lens and retinal layers in the eye and could quantitatively measure changes in normal brain development. Further, diceCT could qualitatively identify ZIKV-infected animals in an unbiased cohort before disease is overt (6 dpi) and can both qualitatively and quantitatively identify changes in regions of the brain in ZIKV-infected animals later during infection (10 dpi), when clinical signs are emerging.

The changes identified are consistent with previous descriptive pathology in mice and humans, which we further extend with quantitative analysis, showing a decline in tissue volume in multiple regions of the brain. Post diceCT, histological Nissl and immunostaining for the microglial marker, Iba1, was successful. Thus, in the future, diceCT may serve as a relatively simple addition to the toolkit for research studies seeking to link *in situ* tissue morphology to detailed cellular and molecular changes, further facilitating our understanding not only of ZIKV-induced brain pathology but also, potentially, of other neurodevelopmental or neurodegenerative disorders.

## Materials and Methods

*ZIKV stocks and infection of neonatal mice.* Viral infections utilised the ZIKV strain PRVABC59, amplified in C6/36 cells with cell culture supernatants harvested, clarified, filtered, and stored at -80°C. Infectious titre was determined by plaque assay on Vero cells and quantitated as a plaque forming unit (pfu) per mL, as previously described [29,50].

One-day old Balb/c pups (n= 23 total) were infected by injection into the body above the milk spot with a 31G insulin needle and 5000 pfu of ZIKV, in a total volume of 10  $\mu$ L, as previously described [29]. Mice were monitored daily for colour and movement. At designated time points post infection (pi), mice were weighed and humanely killed by decapitation. Tissue sample at the site of decapitation was taken for RNA extraction and RT-PCR for ZIKV, as previously described [29]. Whole heads were fixed in 10% (v/v) buffered formalin overnight and thereafter stored in phosphate buffered saline (PBS) at room temperature. Samples were collected for at 3- and 6-days pi (dpi) (n=4 mock, n=2 ZIKV per time point), across 2 different litters, and at 10 dpi for ZIKV and uninfected animals from the same litter (n=3/group). For unbiased blind analysis at 6 dpi, samples reflected n=3 uninfected and n=4 ZIKV infected, within one litter. The study was undertaken in accordance with the Australian Code for the Care and use of Animals for Scientific Purposes (2013), and with approval from the Flinders University Animal Welfare Committee, AEC BIOMED 4707-6 and the Flinders University Institutional Biosafety Committee, Microbiological approval, 2016-07.e1.

*DiceCT staining and scanning.* Fixed specimens were submerged in 3.75% (w/v) B-lugol's solution as described in Dawood *et al.* (2021) to reduce soft-tissue shrinkage [51]. Even penetration of the iodine stain was facilitated by incubation at room temperature on rocker for either approximately 36 hours (h) for specimens at 3 and 6 dpi or 48 h for 10 dpi specimens. Specimens were rinsed with PBS and prepared for scanning by wrapping in foam and PBS-soaked gauze to avoid desiccation. Specimens were subjected to X-ray micro-computed tomography (micro-CT) using a Bruker SkyScan 1276 high resolution micro-CT at Adelaide University Microscopy Facility (Adelaide Health and Medical Centre [AHMS], University of Adelaide, South Australia). Settings were as follows: 90 kV, 200  $\mu$ A, 430 millisecond (ms) exposure time, frame averaging of 2, 0.2° rotation steps and using 0.25 mm aluminium filter. Each specimen was scanned for approximately 90 minutes (min) for a final resolution of 6.5  $\mu$ m (detector resolution at 4032 x 2600 pixels). The radiographs from these scans were reconstructed in NRecon v.2.0 (Bruker, Kontich, Belgium) to acquire 2D cross-section images or 'slices'. The slices were processed in DataViewer, 3D inspection software (Bruker, Kontich, Belgium) to allow for alignment of specimens' X, Y and Z axes.

*Image segmentation, visualisation and quantitation of brain volumes.* Brain segments were defined based on labelled regions marked in the Allen Developing Mouse Brain Reference Atlas [52]. To acquire volume measurements of the whole brain and brain segments, regions were digitally segmented from CT scans with 3D Slicer (www.slicer.org), [53] to create 3D models. The add-on module SlicerMorph [54] was used to import the aligned CT scans into the 3D Slicer program, using the 'ImageStacks' function. This allowed the CT scans to be loaded into the program at a lower resolution, to allow efficient segmentation on a general use computer system. This was appropriate for the easily identifiable brain regions analysed here but would not be recommended when segmenting less visible or finer structures, such as the retina. 3D Slicer's 'Reformat' module was also used to visually reorient images where necessary. The 'Segment Editor' module was used to digitally segment regions of the brain. A region was defined using the '+' function to name and select region colour, and the 'Paint' tool



was used to manually select the region of interest. Regions were manually selected in slices across the X, Y and Z axes and the 'Fill between slices' tool was used to interpolate defined regions between slices. The interpolated region between the manually defined slices was dependent on the rate of change in the region across the number of slices and varied for each region. To obtain the 3D models, the defined segments within the 'Data' module were selected and 'export visible segments to models' was chosen. The generated segmentation models could then be exported from 3D slicer for analysis. Models exported from 3D Slicer were edited in MeshLab v.2021.07 [55] using the 'Surface Reconstruction: Screened Poisson' function [56] to ensure they were manifold and that the volumes of the whole brain and separate regions could be correctly quantified. Volume was calculated using the package Rvcg v.0.22.1 function 'vcgVolume' in the R Statistical Environment v.4.3.1 [57]. Slicer data sets are available on Figshare (10.25451/flinders.26086651).

*Blinded review of 6 dpi scans.* A link to rendered videos from coronal sections were numbered 1-7, and provided to 4 authors for review; two virologists (ECC, JMC) and two rodent neuroanatomists (LMC, LC-P). The author (ALG) who undertook the diceCT analysis was excluded from review. Videos were viewed independently and assigned as uninfected, ZIKV-infected or undetermined, with supporting comments provided.

*Tissue destaining and preparation of sections.* Following diceCT scanning, tissues were destained by submersion in 1% (w/v) sodium thiosulphate on an orbital platform for 3 days to remove the iodine stain, followed by 2 days in deionised water to remove the destaining reagent [58]. Destaining was essential for obtaining good quality tissue sections. Destained tissue was serially treated in 10% then 20% (w/v) sucrose in PBS for 1 h each, and then finally transferred to 30% (w/v) sucrose in PBS overnight, or until the tissues sank to the bottom of the tube. Once cryoprotected, tissues were embedded (OCT compound, TissueTek). 15 µm coronal cryostat sections were mounted onto glass slides, air dried, 30 mins at room temperature then stored in an airtight container at -20°C.

*Immunolabelling and Nissl staining of post diceCT tissue.* Sections from the midbrain were selected for post diceCT analyses. Frozen tissue sections were thawed then rehydrated in PBS, 10 min at room temperature. Antigen retrieval was performed for 20 mins in 10 mM sodium citrate, 0.05% Tween 20, pH 6 that was heated until boiling. Tissue sections were permeabilised with 0.5% (v/v) IGEPAL (Sigma) in PBS for 20 min at room temperature then rinsed 3 times for 5 mins in PBS. Non-specific binding was blocked with 5% (v/v) normal goat sera (NGS) and 2% (w/v) bovine serum albumin (BSA) in PBS for 1 h at room temperature. Tissue sections were immunostained with anti-ionized calcium binding adaptor molecule 1 (Iba1) (rabbit polyclonal, 1:100 dilution, 1 µg/mL, Wako) diluted in 2% (v/v) NGS in PBS in a humidified chamber for 24 h at 4°C. Sections were washed in PBS and bound antibody detected using anti-rabbit Alexa Fluor 555 (ThermoFisher Scientific), diluted in 2% (v/v) NGS in PBS for 1 h at room temperature, protected from the light. Autofluorescence was quenched (ReadyProbes™ tissue autofluorescence quenching kit, ThermoFisher) by post staining incubation with quenching reagent for 5 mins at room temperature. Nuclei were then stained (Hoechst 33342, 5 µg/mL, ThermoFisher Scientific) for 10 min at room temperature protected from the light. Sections were then mounted (ProLong Gold Antifade, ThermoFisher Scientific) and imaged by fluorescent microscopy (VS200 Slide Scanner, Olympus).

Additional serial sections were selected for cresyl violet staining of the Nissl body. Fixed sections were air dried for 1 h at room temperature, then de-fatted by immersion in a 1:1 chloroform:ethanol solution for 3 h. Sections were rehydrated through a series of ethanol dilutions 100%, 95%, and 75% (v/v), and then deionised water for 3 mins. The sections were stained for 10 min at 37°C in 0.1% (w/v) cresyl violet then rinsed under gently running deionised water. Staining was differentiated using 95% ethanol then dehydrated in 100% ethanol, 2x 5 min, and cleared in xylene, 2x 5 min. Stained sections were mounted (DePeX mounting medium) and examined using brightfield microscopy (VS200 Slide Scanner, Olympus).

*Statistical Analyses.* Measurements of mouse body weight were normally distributed (Shapiro-Wilk test) and compared using Student's unpaired *t*-test. Volume data of the whole brain and separate regions were analysed for statistical differences between treatment groups and days post infection in

the R Statistical Environment using a one-way analysis of variance (ANOVA), with Tukey’s multiple comparison test. Significance was set at an alpha level = 0.05. Results were visualised using GraphPad Prism v. 10.0.0.

Results

*DiceCT can track brain development and the impact of ZIKV infection.* Newborn P1 mice were left uninfected or ZIKV-infected. Animals were taken at 3 and 6 dpi, where we know there is increasing viral replication and induction of antiviral and inflammatory host responses with a lack of overt clinical signs [29]. This infection model was also extended to 10 dpi, with a single litter to avoid across litter variation, where half of the litter was left uninfected and half ZIKV-infected, and analysis performed in a blind fashion. Mice that were determined retrospectively to be ZIKV positive by RT-PCR were visibly smaller, with a significantly lower total body weight ( $p=0.007$ ,  $t=5.042$ ,  $df=4$ ) and observable mild hind limb dysfunction, presenting as a mild tremor or reduced ability to traverse a straight line (Table 1). Head measurements tended to be lower, but were not significantly reduced (Table 1). DiceCT staining was performed on whole heads at 3, 6 and 10 dpi (Figure 1A). DiceCT analysis yielded clear discrimination of regions of the developing mouse brain across P4-P11 in uninfected and infected animals (3-10 dpi) (Figure 1A). At this time point, the eyes are still closed, and the lens and retinal layers are clearly visible on imaging. The developing teeth are evident. In general, no clear defects were observed in ZIKV-infected mouse brain at 3 dpi based on visual inspection, although a unilateral gap in the cortical region was visualised in one animal, as shown (Figure 1A). By 6 and 10 dpi, unilateral and bilateral gaps, often at the point of intersection of different regions of the brain and most apparent at the level of the posterior hippocampus, as well as expansion of ventricular spaces, were more widely observed in ZIKV-infected animals. Serial coronal images are shown across the brain of one animal at 10 dpi, with clear pathology in the olfactory bulb and frontal regions of the brain (Figure 1B). Overall, the ZIKV-induced brain pathology was diverse, and no hallmark or characteristic pathology was consistently identified across all ZIKV-infected animals. There was also no evidence for calcifications in ZIKV-infected mice identified by gross morphology at this early time of infection.

**Table 1. Summary of mice at 10 dpi.** Mice in a single litter were left uninfected or ZIKV-infected and blindly allocated mouse ID 1-6, movement analysed, weighed and heads measured at 10 dpi. ZIKV infection status was defined retrospectively by RT-PCR. \*  $p<0.05$ , Student’s unpaired  $t$ -test.

| Mouse ID                       | Weight (g)      | Head length, L, width, W, depth, D (cm) | ZIKV RT-PCR                    | Movement                       |
|--------------------------------|-----------------|---|--------------------------------|--------------------------------|
| 1                              | 6.40            | L=1.9; W=0.8; D=0.6                     | positive                       | Mild hind limb dysfunction     |
| 2                              | 7.50            | L=2.3; W=1; D=1                         | negative                       | normal                         |
| 3                              | 6.64            | L=2.1; W=1.2; D=0.9                     | positive                       | Mild hind limb dysfunction     |
| 4                              | 5.93            | L=2.1; W=0.9; D=0.7                     | positive                       | Mild hind limb dysfunction     |
| 5                              | 7.37            | L=1.8; W=0.7; D=0.8                     | negative                       | normal                         |
| 6                              | 7.34            | L=2.1; W=0.9; D=0.7                     | negative                       | normal                         |
| Mean ± SEM                     | Body Weight (g) | Head Length (cm)                        | Head Width (cm)                | Head Depth (cm)                |
| Mock (2, 5, 6)                 | 7.40 ± 0.05     | 2.17±0.07                               | 1.03±0.09                      | 0.87±0.09                      |
| ZIKV (1, 3, 4)                 | *6.32 ± 0.21    | 1.93±0.09                               | 0.8±0.06                       | 0.7±0.06                       |
| $p=0.007$ , $t=5.042$ , $df=4$ |                 | $p=0.102$ , $t=2.211$ , $df=4$          | $p=0.091$ , $t=2.214$ , $df=4$ | $p=0.189$ , $t=1.581$ , $df=4$ |

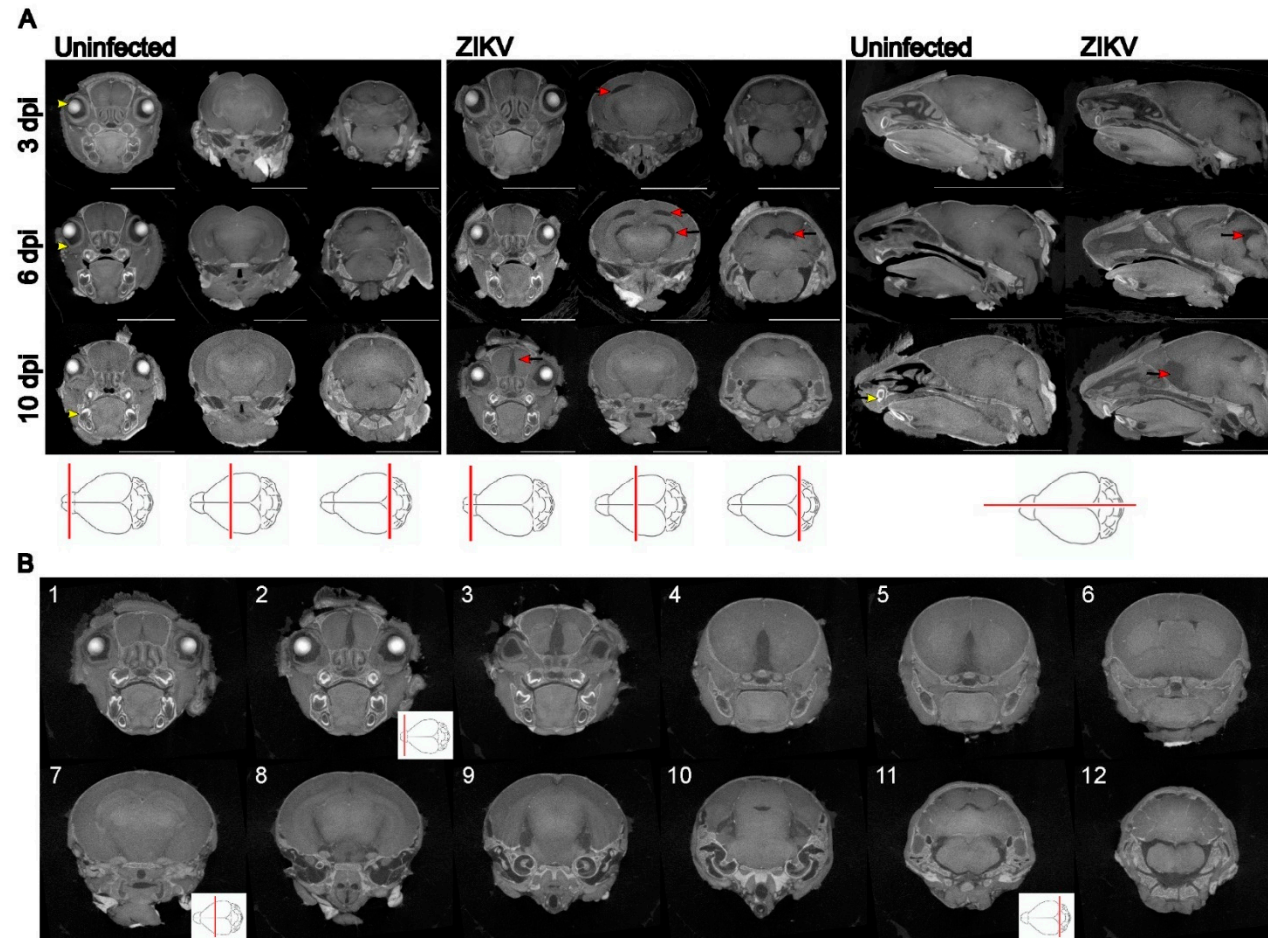


**Figure 1. diceCT imaging of uninfected and ZIKV-infected neonatal mouse heads throughout development.** P1 mice were left uninfected or ZIKV-infected and at the time points indicated, whole heads were collected and subjected to diceCT. **A.** Images across three coronal and one sagittal plane of selected animals are shown (position indicated by red line on brain outline image below), from animals at 3 and 6 dpi (n=4 mock, n=2 ZIKV per time point), and 10 dpi (n=3/group). Examples of lens, retina and teeth are indicated by yellow arrows. Red arrows highlight examples of ZIKV-induced pathology. Scale bars, 0.5 cm (coronal); 1cm (sagittal) **1 B.** serial coronal sections from one 10 dpi ZIKV-infected animal. Video compilation of images are available at Figshare (10.25451/flinders.26086651).

Image outputs were subjected to quantitative analysis. Software programs, CTAn and CTvol (Bruker-microCT), Drishti (Limaye, 2012), Avizo (Thermofisher Scientific), VGStudio Max (Volume Graphics), Imaris (Oxford Instruments) and 3D Slicer were assessed for ease of use and availability for a routine virology research laboratory in quantitative analysis of CT images. 3D slicer was chosen as an intuitive, free, open-source program that can handle large data sets without specialised computing power and has good online supporting tutorial resources [53]. The micro-CT files were converted to produce high-definition 3D outputs that allow visualisation and quantitation of the surface volumes and internal tissue detail to undertake manual and semi-automated segmenting. Scans were reconstructed and resulting images segmented and analysed [53], with confident segmentation of the brain into 7 regions: the olfactory bulb, cerebrum, hippocampus, interbrain (comprising thalamus and hypothalamus), midbrain, cerebellum and hindbrain (including brain stem). A representative schema illustrating the segmented regions is shown (Figure 2A, B). Quantitation of whole brain volume demonstrated a significant increase over developmental time in uninfected mice, as expected ( $p=0.0001$ ,  $F=68.5$ ,  $df(5, 5)$ ). There was a significant increase from 3 to 6 dpi in ZIKV-infected mice ( $p=0.0008$ ) and a significant decline between 6 and 10 dpi ( $p=0.0006$ ) in total brain volume (Figure 2C). Total brain volume was not significantly different at 3 and 6 dpi for ZIKV-infected compared to uninfected mice, but total brain volume was reduced at 10 dpi in ZIKV-infected mice, relative to uninfected mice at the same time point ( $p=0.0002$ ), (Figure 2C).

The same pattern of growth and impact of ZIKV was seen in other regions of the brain (Figure 3). In the cerebrum ( $p<0.0001$ ,  $F=67.12$ ,  $df(5, 10)$ ) and olfactory bulb ( $p<0.0001$ ,  $F=36.10$ ,  $df(5, 10)$ ), volumes increased from 3, 6 to 10 dpi in uninfected mice. Volumes similarly increased from 3-6 dpi in ZIKV-infected mice, but there was a significant decline in volume by 10 dpi ( $p<0.0001$ ;  $p=0.0181$ , respectively). Cerebrum and olfactory bulb volume was also significantly reduced in ZIKV-infected compared to uninfected mice at 10 dpi ( $p<0.0001$ ;  $p=0.0011$ , respectively) (Figure 3). In the hippocampus ( $p=0.0030$ ,  $F=7.916$ ,  $df(5, 10)$ ), interbrain ( $p=0.0013$ ,  $F=9.902$ ,  $df(5, 10)$ ) and cerebellum ( $p<0.0001$ ,  $F=45.68$ ,  $df(5, 10)$ ), volumes also increased from 3-10 dpi in uninfected animals, and were reduced in ZIKV-infected mice at 10 dpi compared to uninfected mice at the same time point ( $p=0.0383$ ;  $p=0.0100$ ;  $p=0.0004$ , respectively) (Figure 3). For midbrain ( $p=0.0024$ ,  $F=8.384$ ,  $df(5, 10)$ ) and hindbrain ( $p=0.0514$ ,  $F=3.291$ ,  $df(5, 10)$ ), there was no significant increase in volume over time in uninfected animals. For the midbrain, uninfected mice at 10 dpi show no increase in volume compared to 6 dpi, and a significant reduction in ZIKV-infected mice at 10 dpi compared to uninfected at this same time point ( $p=0.0098$ ). For the hindbrain, no volume changes were significant, although notably one ZIKV-infected sample at 6 dpi was noted post-diceCT analysis to be missing the brain stem, presumably during the collection process (Figure 3).



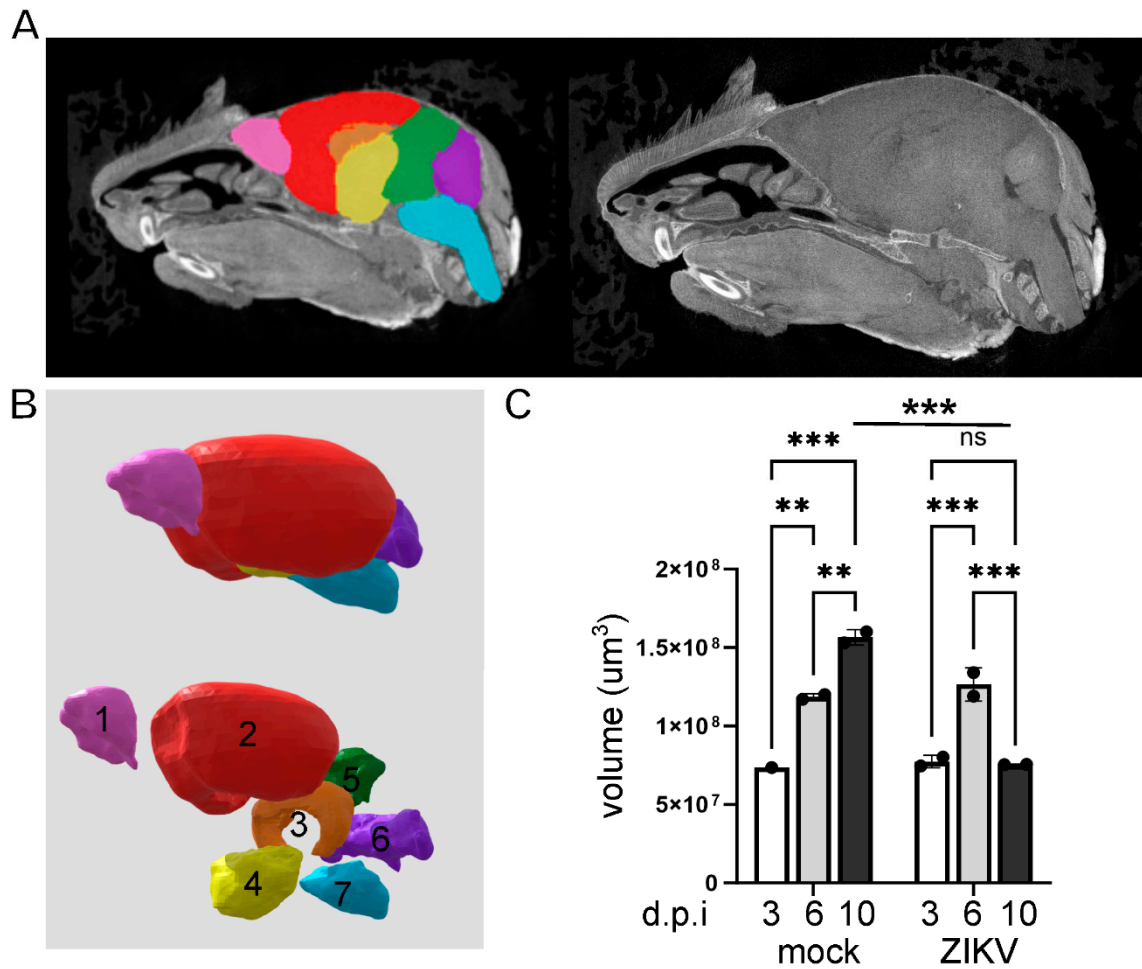


**Figure 2.** Brain segmentation and quantitation of total brain volumes throughout development in uninfected and ZIKV-infected mice. P1 mice were left uninfected or ZIKV-infected and, at the time points indicated, whole heads were collected and subjected to diceCT. Images were rendered, brains segmented and volume quantitated. A. sagittal diceCT image with segmented regions of the brain superimposed; B. segmented brain regions 1= olfactory bulb, 2 = cerebrum, 3 = hippocampus, 4 = interbrain (thalamus and hypothalamus), 5 = midbrain, 6 = cerebellum, 7 = hindbrain and brain stem; C. Total brain volume. \*  $p < 0.05$ , one-way ANOVA, Tukey's multiple comparison test. 3 and 6 dpi (n=4 mock; n=2 ZIKV per time point), and 10 dpi (n=3/group).

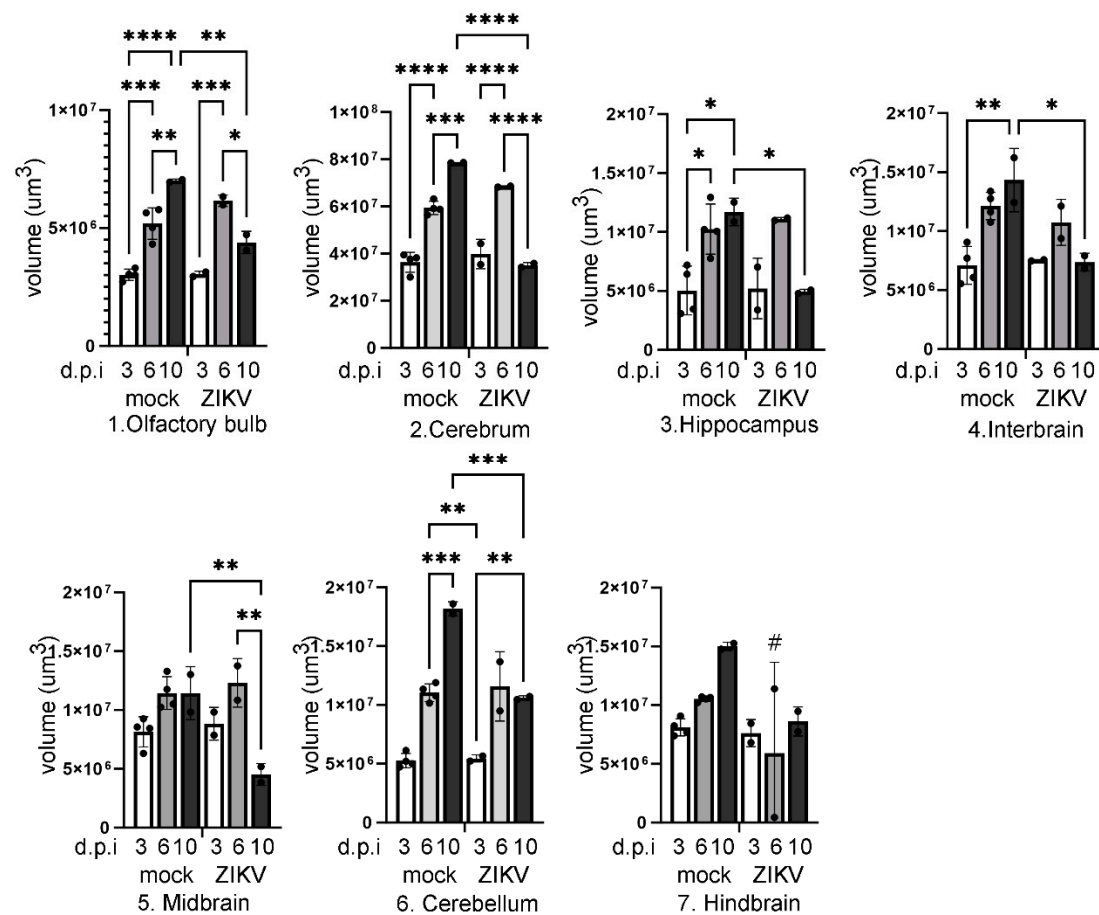


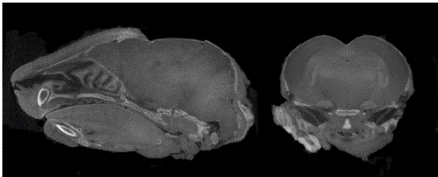
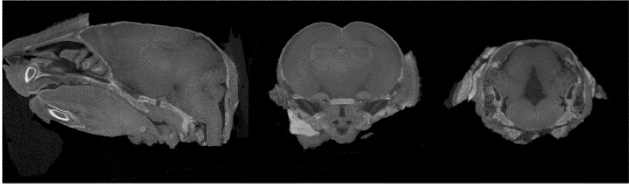
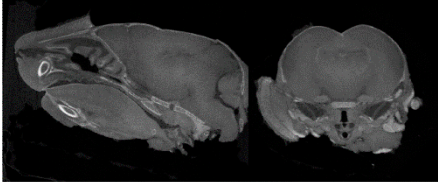
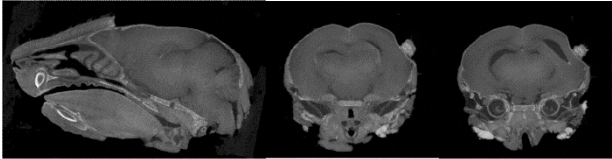
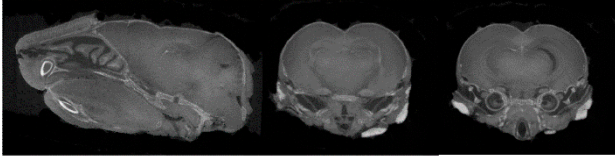
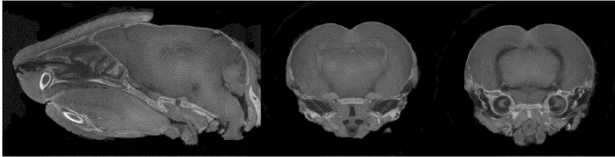
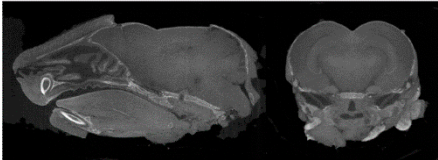
**Figure 3.** Quantitation of changes in volumes of different regions of the brain throughout development in uninfected (UI) and ZIKV-infected mice. P1 mice were left uninfected or ZIKV-infected and at the time points indicated, whole heads were collected and subjected to diceCT. Images were rendered and brains regions: 1 (olfactory bulb), 2 (cerebrum), 3 (hippocampus), 4 (interbrain), 5 (midbrain), 6 (cerebellum) and 7 (hindbrain) were segmented as outlined in Figure 2, and volume quantitated. \*  $p < 0.05$ , one-way ANOVA, Tukey's multiple comparison test. # = unreliable due to loss of brain stem at sample collection.

Although quantitative brain measurements at 6 dpi were not significantly different between uninfected and ZIKV-infected animals, our qualitative analysis suggested that defects might be visually evident at this time point, although with diverse pathology. Given this, the ability to utilise diceCT to visually or quantitatively identify ZIKV-infected animals in a blind cohort at 6 dpi, before disease is clinically overt, was assessed. Neonatal P1 mice from a single litter were left uninfected ( $n=3$ ) or ZIKV-infected ( $n=4$ ) and at 6 dpi were subjected to diceCT analysis. Independent visual analysis of images by four reviewers with diverse expertise in virology and rodent neuroanatomy, identified consistent morphological differences in animal numbers 2, 4 and 6 that penetrated multiple layers of the brain (Figure 4, Table 2). All reviewers identified animal number 1 definitively as uninfected. Three of four authors identified animal 5 as ZIKV-infected, but with some reservations, and, similarly, animals 3 and 7 were deemed to be likely uninfected or presented some uncertainty (Table 2). Quantitative analysis was performed on segmented brain images, per Figure 2. In line with the blind ratings, animal 4 tended to reflect smaller measures in the interbrain, midbrain and cerebellum. Brain volumes, however, were not significantly different across the cohort, and samples did not cluster well into 2 distinct groups, that could suggest alignment with either uninfected or ZIKV-infected animals (Figure 5). The biggest variability and changes were observed at the level of

the midbrain or posterior hippocampus both visually and in the quantitative analysis. Thus, diceCT imaging could qualitatively identify most ZIKV-infected animals with certainty but cannot quantitatively predict ZIKV-infection in a blind cohort, prior to clinical presentation of disease.

**Table 2. Summary of blinded scoring of mixed 6 dpi cohort.** UI = uninfected; UD = undetermined. Unequivocal assignments for ZIKV are highlighted.

| Mouse ID | Reviewer 1   | Reviewer 2   | Reviewer 3   | Reviewer 4   |
|----------|--|--|--|--|
| 1        | No pathological findings noted                               | No pathological findings noted   | No pathological findings noted   | No pathological findings noted   |
|          | UI   | UI   | UI   | UI   |
|          |  |  |  |  |
| 2        | Major gap at rear of brain                                   | Asymmetrical gaps at the level of the hippocampus/thalamus   | Asymmetrical, apparent volume loss in the hippocampus  | Asymmetrical, increased space between hippocampal region and thalamus and towards the hind brain                         |
|          | ZIKV   | ZIKV   | ZIKV   | ZIKV   |
|          |  |  |  |  |
| 3        | No pathological findings noted                               | Some gaps, but no asymmetrical volume loss   | No pathological findings noted   | Slight gaps between hippocampal region and thalamus  |
|          | probably UI  | UI   | UI   | probably UI  |
|          |  |  |  |  |
| 4        | Multiple asymmetrical gaps, penetrating across midbrain      | Clear asymmetrical gaps between structures, with majority of abnormalities around thalamus and hippocampus, continuing through the posterior brain | Very clear asymmetrical abnormalities, particularly at level of posterior hippocampus, and continuing more posteriorly                           | Gaps between hippocampus and cortex (right) and thalamus (left); Gap (right) appears to go through majority of the brain |
|          | ZIKV   | ZIKV   | ZIKV   | ZIKV   |
|          |  |  |  |  |
| 5        | Maybe minor anomalies;                                       | Asymmetrical gaps between hippocampus and thalamus   | Abnormality in region anterior to nuc accumbens and at level of striatum (less defined); Clear asymmetry at the level of the poster hippocampus; | Gap in between hippocampal region and thalamus   |
|          | UD   | ZIKV   | ZIKV   | probably ZIKV  |
|          |  |  |  |  |
| 6        | Symmetrical gaps, penetrating across images through midbrain | Clear gaps at hippocampus, continuing throughout posterior brain   | Very clear abnormalities, particularly at level of posterior   | Gap in between hippocampal region and thalamus on left and right side, which   |
|          |  |  |  |  |
|          |  |  |  |  |

|                          |  |  |   |   |   |
|--------------------------|--|--|---|---|---|
| ZIKV                     |  | ZIKV   |   | hippocampus and<br>extending posteriorly  | runs through majority<br>of brain                         |
|                          |  |  |   | ZIKV  | ZIKV  |
| Maybe minor<br>anomalies |  | Minor abnormalities  |   | Some minor<br>abnormality, which<br>may be an imaging<br>artifact or normal<br>anatomical variation | Slight gap between<br>hippocampal region<br>and thalamus; |
| 7                        |  |  |   |   |   |
| UD                       |  | UI   |   | UD  | probably UI   |
| Animal #;<br>weight (g)  |  | A  | B | C   |   |
| 1;<br>5.0 g              |  |     |   |   |   |
| 2;<br>5.23 g             |  |   |   |   |   |
| 3;<br>4.87 g             |  |   |   |   |   |
| 4;<br>5.07 g             |  |  |   |   |   |
| 5;<br>5.08 g             |  |  |   |   |   |
| 6;<br>5.13 g             |  |  |   |   |   |
| 7;<br>5.09 g             |  |   |   |   |   |

**Figure 4. diceCT imaging of the brain at 6 dpi in a blind cohort of uninfected and ZIKV-infected animals.** P1 mice from a single litter were left uninfected (n=3) or ZIKV-infected (n=4), then at 6 dpi, whole heads were taken and subjected to diceCT in a blinded fashion. **A.** single sagittal; **B.** coronal



section from each animal is shown across the midbrain, as in Figure 1; C. regions of identified significant pathology. Numbers 1-7 represent individual mice, and weights (g) at 6 dpi are indicated. Images compiled into videos are available at Figshare 10.25451/flinders.26086651.

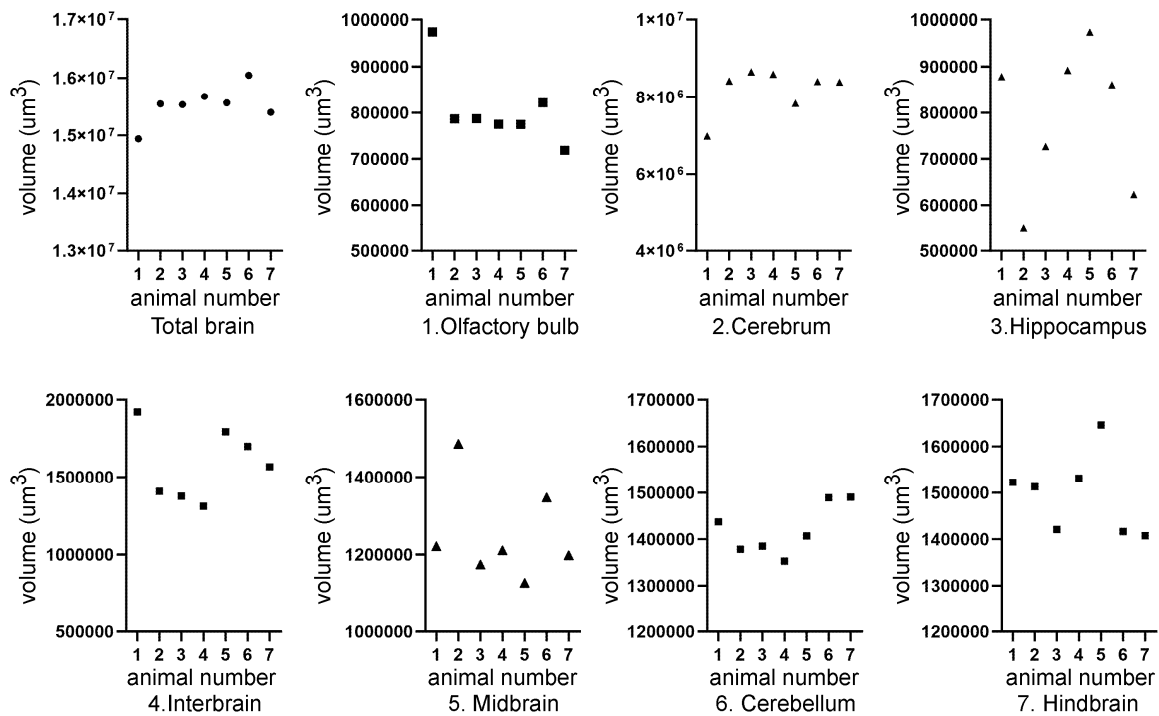


**Figure 5.** Quantitation of changes in volumes of different regions of the brain at 6 dpi in a blind cohort of uninfected and ZIKV-infected mice. P1 mice from a single litter were left uninfected (n=3) or ZIKV (n=4), then at 6 dpi subjected to diceCT in a blinded fashion as in Figure 4, with segmentation and quantitation of brain volumes as in Figure 2A. Numbers 1-7 represent individual mice.

*Tissue can be utilised post diceCT for traditional histology and immunostaining.* DiceCT defines tissue structures in 3D spatial relationship, and it would be informative to link this to changes at a cellular level. The utility of the diceCT processed tissue for subsequent RNA analysis and traditional histological and immunostaining was assessed here. Samples post diceCT that had been stored in PBS were destained to remove the iodine. Sections of brain cortical tissue were sampled, and RNA extracted by traditional Trizol method, or a commercial kit designed for RNA recovery from formalin fixed tissue specimens. Spectrometry analysis of recovered RNA demonstrated poor yields and quality, as judged by A260/280 nm. A trial RT-PCR for the housekeeping gene, GAPDH, on these samples was not successful (data not shown). Destained tissue was also processed for traditional embedding. Specimens that were not extensively destained prior to embedding ‘shattered’ and intact good quality sections were not obtained. Conversely, however, extensive destaining prior to sucrose treatment and OCT embedding resulted in successful sectioning. Nissl and immunofluorescent staining for the macrophage/microglial marker, Iba1, were both successful (Figure 6A, B). Staining for Iba1 was chosen as an exemplar antigen, as it is widely expressed across multiple regions of the brain, with positive cells having distinct morphology, including round immature microglia and more mature cells with distinct branches and processes [59]. Immunostaining was of appropriate quality to yield good resolution of images but did lack some clarity in areas (Figure 6B). The soma and processes of Iba1 positive cells in the cortex and hippocampus reflected the expected diversity of morphological microglial classifications at this developmental time point, including both large round cell cells and smaller cells with visually distinct processes. Particularly intense staining of Iba1 positive cells was seen along the edges of the cortex, potentially representing cells in vessels or meninges.

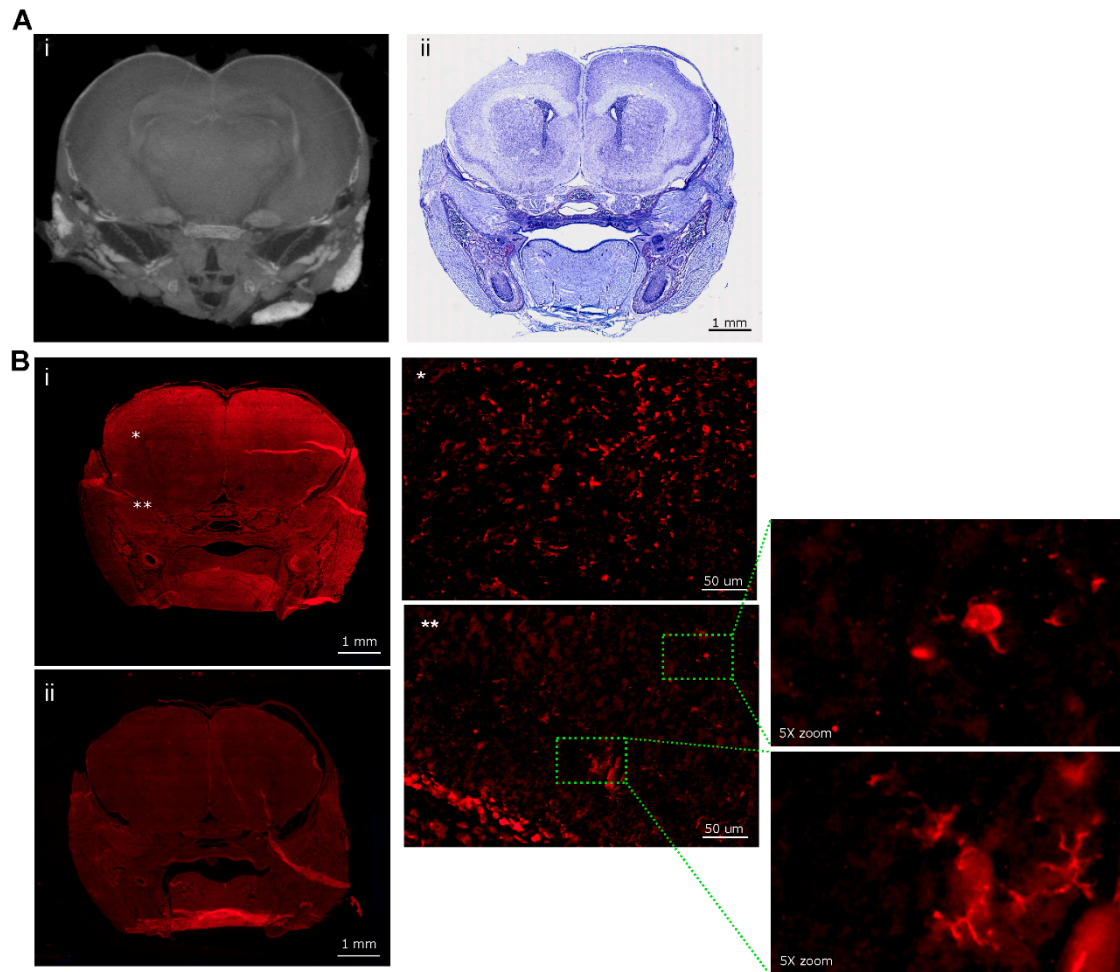


**Figure 6. Post diceCT tissue analysis.** A. Following (i) diceCT analysis, tissue was destained, embedded and coronal sections from the midbrain analysed by (ii) Nissl staining; B. (i) immunofluorescent analysis for Iba1; (ii) no antibody control; Images were collected using a VS200 Slide Scanner. Optical zoom are shown at \* in the hippocampus and \*\* the outer cortex from section (i), with further zoom of regions as indicated by green dotted box and lines.

## Discussion

While a lot is known about ZIKV at a cellular level, the relationship between interacting cells and within specific regions of the brain throughout infection and brain development are less well described. The rarity of clinical material from ZIKV-affected brains makes *in vivo* laboratory models of significant value. The diceCT technique applied here to the developing mouse brain and in the context of ZIKV has provided resolution of different soft tissue regions of the brain, in relation to each other *in situ*, and has analysed the impact over early postnatal development (P4, P7 and P11), equating to early infection time points (3, 6 and 10 dpi). Quantitatively, in uninfected mice, there is a clear and significant increase in volume of the total brain, cerebrum, hippocampus and olfactory bulb with time, indicating growth of these regions during the P4-P11 stages of development, and consistent with the a major post-natal increase in brain volume in rodents out to P20 [37]. For the cerebellum, the significant volume increase was between P7 and P11, suggesting a more significant growth phase at this later time. This is consistent with MEMRI quantitation of these regions over the same time period, with greater rate of volume increase of the cerebellum from P6 [49]. This also aligns with the later development of granule cells (GC) neurons in the hippocampus and olfactory bulb and in the cerebellum in the first 2 weeks postnatally [37,60]. For the midbrain and hindbrain, trends for volume increases are evident, but these did not reach significance and would benefit from increased animal numbers for this quantitative analysis.

At 3 and 6 dpi in ZIKV-infected mice, the virus is replicating and induction of inflammatory responses is ongoing [29]; however, the mice at this time are physically indistinguishable in behaviour or size, and not quantitatively different by diceCT imaging from uninfected mice. Notably, however, morphological defects could be visually detected by assessors with expertise in rodent neuroanatomy in some individual ZIKV-infected animals at 6 dpi. When a litter of uninfected and ZIKV-infected animals were blindly analysed at 6 dpi, three out of four mice were definitively identified by four independent researchers, and a remaining fourth mouse was identified by three out of four researchers as ZIKV-infected. The impact of ZIKV-infection became more pronounced with time, with 10 dpi, ZIKV-infected mice significantly smaller with the onset of clinical signs. Visually, the ZIKV-induced pathology at 6 and 10 dpi was diverse, with changes observed in multiple regions of the brain, as is also reported in ZIKV-infected babies [5,11,12,14]. The ZIKV morphologies observed in the neonatal mouse model included ventriculomegaly, as previously described [30,31,34]. Interestingly, expansion of ventricular spaces was seen at 6 dpi, without quantitative reduction in any tissue volume, suggesting this could reflect fluid accumulation and a cellular infiltrate due to inflammatory response. At 10 dpi quantitative volume measures in the total brain and all other brain regions, except hindbrain were significantly reduced in relation to uninfected mice. The brain volumes in 10 dpi ZIKV-mice were also reduced relative to 6 dpi and were not significantly different compared to 3 dpi ZIKV-infected mice. This is suggestive of tissue loss and is consistent with cell killing, as previously observed for neurons and NPC [25] and with detection of cleaved caspase 3 and fluoro-Jade in the cortex, hippocampus and cerebellum of ZIKV-infected neonatal mice [34] as well as with neuronal losses observed previously in ZIKV-infected cells and brains [22,23,25]. The volumes of the cerebrum and cerebellum were reduced in ZIKV-infected animals. Functional loss within the cerebellum or in connections with the cerebral cortex are consistent with the onset of motor dysfunction at 10 dpi in ZIKV-infected mice and align with the timing of development of GC neurons and interneurons in these brain regions [60]. Here, diceCT imaging has not resolved neuronal linkages between regions of the brain, but this could be specifically investigated in the future by immunostaining for neuronal markers or retrograde tracer studies, pending feasibility of these methods post-diceCT. Quantitative analysis of the midbrain, an important site of progenitor cells, including radial glial cells for neurons in the cortex was also of significant interest [37]. Analysis demonstrated a trend towards volume increases in the midbrain from 3-6 dpi in both uninfected and ZIKV-infected animals. There was no further increase in volume in uninfected mice at 10 dpi, suggesting reduction of progenitor expansion at this point in development, but midbrain volume decreased significantly in 10 dpi ZIKV-infected animals, again suggestive of cell death. Cell death and neurodegeneration could be specifically assessed, as previously by caspase-3 or fluoro-Jade staining [34], pending compatibility with post diceCT tissue. The timing of the onset of visual pathology at 6 dpi but quantitative loss of brain volumes in multiple regions later at 10 dpi is mechanistically interesting. This could reflect cell killing of progenitor cells at 6 dpi, that manifests as reduced brain volumes at 10 dpi due to a lack of progenitor cell numbers to migrate and expand to these multiple brain regions during later development, rather than viral killing of pre-formed brain regions. Additionally, our qualitative observations were more pronounced in the frontal-midbrain or around the hippocampus, perhaps also reflecting a role of the normal posterior-anterior process of myelination that could protect the developing brain from injury [37]. Changes in the hindbrain and cerebellum are also of future interest, since seizures are reported in later stages of this mouse model of ZIKV infection [35], and caudal or morphologies of the rhombencephalon are strongly associated with epilepsy in CZS [61]. Overall, the findings of ZIKV-induced reduction in volume of multiple regions of the brain is consistent with prior description of diffuse and diverse ZIKV infection in NPC, astrocytes and neurons, across multiple regions of the brain, *in vitro* and in this mouse model [22,31].

While our previous work has demonstrated measurable changes in the layers of the retina at 6 dpi in this model by traditional histology [29], no major visually apparent changes in the retina or eye were detected. This remains to be quantitatively assessed. Interestingly, ZIKV has been recently reported to infect and kill cells of the developing ear [62]. The auditory canals can be visualised in

our diceCT images and, hence, this is also an area of interest in the future for more detailed analysis of this image set, to potentially define a laboratory model of hearing-loss in ZIKV-affected newborns.

Prior to undertaking diceCT, it was hoped that the iodine contrast could resolve potential calcifications as reported in ZIKV-infected babies, but these findings were not evident in our study, either macroscopically or via diceCT. This is likely due to the formation of calcifications as result of longer-term impact of cell death in the brain, and is seen at 3-4 months post infection in a neonatal mouse model of ZIKV-infection, microscopically and macroscopically on the surface of the brain [34]. It may be that the timepoints investigated in the current study were too early to see these changes. Alternatively, this inability to detect calcifications may be due to limitations of the diceCT technique itself with loss of contrast for low density deposits, such as calcium, compared to soft tissue in diceCT tissue. Micro-CT alone may be better for specifically analysing this pathology.

Of note, our study successfully utilised post diceCT tissues for both traditional histology and immunostaining including Nissl staining and Iba1 immunostaining. Importantly, however, the tissue must be thoroughly cleared of iodine and de-stain, otherwise the sample is brittle and hard to section, leading to the shattering observed in the current work. The exemplar immunostain used in the current work, Iba1, indicated that the tissue may have lost some integrity during the diceCT process, but nonetheless was still able to detect a diversity of microglial morphology, as is expected with embryonic and early post-natal immature proliferative microglia transitioning towards the ramified mature adult state [63–65]. Staining was particularly strong in the meninges and could reflect perivascular macrophages or trafficking microglia [66]. While some optimisation of the preparation process may be needed to maximise tissue and antigen integrity, the methodology still offers the benefit of linking 3D changes defined by diceCT to 2D cellular detail, without a need for 3D stitching of stained images and with analysis undertaken on the exact same tissue. Unfortunately, however, good quality RNA was not able to be extracted using current methodology, limiting the ability to link 3D changes with alterations in molecular gene expression, another area of significant interest, without further methodological refinement.

Importantly, beyond ZIKV, diceCT has broader applicability to study the brain in other mouse neurological models, particularly neurodevelopmental disorders, where imaging in 3D and progressively with time are of interest [67]. The iodine staining and micro-CT analysis is amenable to broad applicability in laboratory settings, with inexpensive and easy staining protocols, as well as readily available and relative accessibility of micro-CT equipment in many core imaging facilities. Further, the programs used for quantitation are developing and becoming easier for non-experts to use in a time efficient manner. The most time-consuming aspect of this study was the segmentation process. To address this, there is the potential to develop automated segmentation using 3D slicer [68]. Artificial intelligence (AI) training of data in relation to a specific model, such as differences between the typically developing mouse and that infected with ZIKV, will empower finer detail and efficiencies in brain segmentation.

Overall, this study has applied diceCT, to define early morphological changes in the developing mouse brain and the impact of ZIKV on this. The validity of diceCT in this setting is supported by the consistency of findings with the existing literature, while the added benefit of 3D information and flexibility to align with other laboratory methodology will assist the logistics of including diceCT analysis into a modern research plan. Incorporating diceCT will impact our ability to link the overall anatomical pathology to specific cellular and molecular changes, in a context that retains the spatial interactions within the 3D of the brain to improve our wholistic definition of ZIKV-models of pathology and disease.

**Data Availability Statement:** The data presented in this study are openly available in Figshare repository at 10.25451/flinders.26086651 and includes video compilations and datafiles for 3D slicer segmentation analysis.

**Acknowledgements:** Thank-you to Dr Agatha Labrinidis and Adelaide Microscopy for the use of the micro-CT scanner and assistance in scanning and post-processing. Thank-you to Dr Jaimi A. Gray for assistance in diceCT protocols and advice in programs for visualisation and analysis. Funding for this study was provided by the Channel 7 Children's Research Foundation, Research Grant Program, 23-27474146.



## References

1. Musso, D.; Gubler, D. J., Zika Virus. *Clin Microbiol Rev* **2016**, 29, (3), 487-524.
2. Panchaud, A.; Stojanov, M.; Ammerdorffer, A.; Vouga, M.; Baud, D., Emerging Role of Zika Virus in Adverse Fetal and Neonatal Outcomes. *Clin Microbiol Rev* **2016**, 29, (3), 659-94.
3. Honein, M. A., Recognizing the Global Impact of Zika Virus Infection during Pregnancy. *N Engl J Med* **2018**, 378, (11), 1055-1056.
4. Pierson, T. C.; Diamond, M. S., The emergence of Zika virus and its new clinical syndromes. *Nature* **2018**, 560, (7720), 573-581.
5. Hoen, B.; Schaub, B.; Funk, A. L.; Ardillon, V.; Boullard, M.; Cabie, A.; Callier, C.; Carles, G.; Cassadou, S.; Cesaire, R.; Douine, M.; Herrmann-Storck, C.; Kadhel, P.; Laouenan, C.; Madec, Y.; Monthieux, A.; Nacher, M.; Najjioullah, F.; Rousset, D.; Ryan, C.; Schepers, K.; Stegmann-Planchard, S.; Tressieres, B.; Volumenie, J. L.; Yassinguez, S.; Janky, E.; Fontanet, A., Pregnancy Outcomes after ZIKV Infection in French Territories in the Americas. *N Engl J Med* **2018**, 378, (11), 985-994.
6. Freitas, D. A.; Souza-Santos, R.; Carvalho, L. M. A.; Barros, W. B.; Neves, L. M.; Brasil, P.; Wakimoto, M. D., Congenital Zika syndrome: A systematic review. *PLoS One* **2020**, 15, (12), e0242367.
7. DeSilva, M.; Munoz, F. M.; Sell, E.; Marshall, H.; Tse Kawai, A.; Kachikis, A.; Heath, P.; Klein, N. P.; Oleske, J. M.; Jehan, F.; Spiegel, H.; Nesin, M.; Tagbo, B. N.; Shrestha, A.; Cutland, C. L.; Eckert, L. O.; Kochhar, S.; Bardaji, A.; Brighton Collaboration Congenital Microcephaly Working, G., Congenital microcephaly: Case definition & guidelines for data collection, analysis, and presentation of safety data after maternal immunisation. *Vaccine* **2017**, 35, (48 Pt A), 6472-6482.
8. Mlakar, J.; Korva, M.; Tul, N.; Popovic, M.; Poljsak-Prijatelj, M.; Mraz, J.; Kolenc, M.; Resman Rus, K.; Vesnaver Vipotnik, T.; Fabjan Vodusek, V.; Vizjak, A.; Pizem, J.; Petrovec, M.; Avsic Zupanc, T., Zika Virus Associated with Microcephaly. *N Engl J Med* **2016**, 374, (10), 951-8.
9. Marban-Castro, E.; Gonce, A.; Fumado, V.; Romero-Acevedo, L.; Bardaji, A., Zika virus infection in pregnant women and their children: A review. *Eur J Obstet Gynecol Reprod Biol* **2021**, 265, 162-168.
10. Mulkey, S. B.; Arroyave-Wessel, M.; Peyton, C.; Bulas, D. I.; Fourzali, Y.; Jiang, J.; Russo, S.; McCarter, R.; Msall, M. E.; du Plessis, A. J.; DeBiasi, R. L.; Cure, C., Neurodevelopmental Abnormalities in Children With In Utero Zika Virus Exposure Without Congenital Zika Syndrome. *JAMA Pediatr* **2020**, 174, (3), 269-276.
11. Ghosh, S.; Salan, T.; Riotti, J.; Ramachandran, A.; Gonzalez, I. A.; Bandstra, E. S.; Reyes, F. L.; Andreansky, S. S.; Govind, V.; Saigal, G., Brain MRI segmentation of Zika-Exposed normocephalic infants shows smaller amygdala volumes. *PLoS One* **2023**, 18, (7), e0289227.
12. Mejdoubi, M.; Monthieux, A.; Cassan, T.; Lombard, C.; Flechelles, O.; Adenet, C., Brain MRI in Infants after Maternal Zika Virus Infection during Pregnancy. *N Engl J Med* **2017**, 377, (14), 1399-1400.
13. Melo, A. S.; Aguiar, R. S.; Amorim, M. M.; Arruda, M. B.; Melo, F. O.; Ribeiro, S. T.; Batista, A. G.; Ferreira, T.; Dos Santos, M. P.; Sampaio, V. V.; Moura, S. R.; Rabello, L. P.; Gonzaga, C. E.; Malinger, G.; Ximenes, R.; de Oliveira-Szejnfeld, P. S.; Tovar-Moll, F.; Chimelli, L.; Silveira, P. P.; Delvechio, R.; Higa, L.; Campanati, L.; Nogueira, R. M.; Filippis, A. M.; Szejnfeld, J.; Voloch, C. M.; Ferreira, O. C., Jr.; Brindeiro, R. M.; Tanuri, A., Congenital Zika Virus Infection: Beyond Neonatal Microcephaly. *JAMA Neurol* **2016**, 73, (12), 1407-1416.
14. Ribeiro, B. N. F.; Muniz, B. C.; Gasparetto, E. L.; Ventura, N.; Marchiori, E., Congenital Zika syndrome and neuroimaging findings: what do we know so far? *Radiol Bras* **2017**, 50, (5), 314-322.
15. Schuler-Faccini, L.; Del Campo, M.; Garcia-Alix, A.; Ventura, L. O.; Boquett, J. A.; van der Linden, V.; Pessoa, A.; van der Linden Junior, H.; Ventura, C. V.; Leal, M. C.; Kowalski, T. W.; Rodrigues Gerzson, L.; Skilhan de Almeida, C.; Santi, L.; Beys-da-Silva, W. O.; Quincozes-Santos, A.; Guimaraes, J. A.; Garcez, P. P.; Gomes, J. D. A.; Vianna, F. S. L.; Anjos da Silva, A.; Fraga, L. R.; Vieira Sanseverino, M. T.; Muotri, A. R.; Lopes da Rosa, R.; Abeche, A. M.; Marcolongo-Pereira, C.; Souza, D. O., Neurodevelopment in Children Exposed to Zika in utero: Clinical and Molecular Aspects. *Front Genet* **2022**, 13, 758715.
16. de Fatima Vasco Aragao, M.; van der Linden, V.; Brainer-Lima, A. M.; Coeli, R. R.; Rocha, M. A.; Sobral da Silva, P.; Durce Costa Gomes de Carvalho, M.; van der Linden, A.; Cesario de Holanda, A.; Valenca, M. M., Clinical features and neuroimaging (CT and MRI) findings in presumed Zika virus related congenital infection and microcephaly: retrospective case series study. *BMJ* **2016**, 353, i1901.
17. Mulkey, S. B.; Bulas, D. I.; Vezina, G.; Fourzali, Y.; Morales, A.; Arroyave-Wessel, M.; Swisher, C. B.; Cristante, C.; Russo, S. M.; Encinales, L.; Pacheco, N.; Kousa, Y. A.; Lanciotti, R. S.; Cure, C.; DeBiasi, R. L.; du Plessis, A. J., Sequential Neuroimaging of the Fetus and Newborn With In Utero Zika Virus Exposure. *JAMA Pediatr* **2019**, 173, (1), 52-59.
18. Niemeyer, B.; Hollanda, R.; Muniz, B.; Marchiori, E., What We Can Find Beyond the Classic Neuroimaging Findings of Congenital Zika Virus Syndrome? *Eur Neurol* **2020**, 83, (1), 17-24.
19. de Paula Freitas, B.; Ventura, C. V.; Maia, M.; Belfort, R., Jr., Zika virus and the eye. *Current opinion in ophthalmology* **2017**, 28, (6), 595-599.
20. Oliver, G. F.; Carr, J. M.; Smith, J. R., Emerging infectious uveitis: Chikungunya, dengue, Zika and Ebola-A review. *Clinical & experimental ophthalmology* **2018**.

21. Marcelino, B. L. M.; Dos Santos, B. L.; Doerl, J. G.; Cavalcante, S. F.; Maia, S. N.; Arrais, N. M. R.; Zin, A.; Jeronimo, S. M. B.; Queiroz, C.; Hedin-Pereira, C.; Sequerra, E. B., Zika virus infection histories in brain development. *Dis Model Mech* **2023**, 16, (7).
22. He, Z.; An, S.; Chen, J.; Zhang, S.; Tan, C.; Yu, J.; Ye, H.; Wu, Y.; Yuan, J.; Wu, J.; Zhu, X.; Li, M., Neural progenitor cell pyroptosis contributes to Zika virus-induced brain atrophy and represents a therapeutic target. *Proc Natl Acad Sci U S A* **2020**, 117, (38), 23869-23878.
23. Garcez, P. P.; Loiola, E. C.; Madeiro da Costa, R.; Higa, L. M.; Trindade, P.; Delvecchio, R.; Nascimento, J. M.; Brindeiro, R.; Tanuri, A.; Rehen, S. K., Zika virus impairs growth in human neurospheres and brain organoids. *Science* **2016**, 352, (6287), 816-8.
24. Komarasamy, T. V.; Adnan, N. A. A.; James, W.; Balasubramaniam, V., Zika Virus Neuropathogenesis: The Different Brain Cells, Host Factors and Mechanisms Involved. *Frontiers in immunology* **2022**, 13, 773191.
25. Li, C.; Xu, D.; Ye, Q.; Hong, S.; Jiang, Y.; Liu, X.; Zhang, N.; Shi, L.; Qin, C. F.; Xu, Z., Zika Virus Disrupts Neural Progenitor Development and Leads to Microcephaly in Mice. *Cell Stem Cell* **2016**, 19, (1), 120-6.
26. Rubio-Hernandez, E. I.; Comas-Garcia, M.; Coronado-Ipina, M. A.; Colunga-Saucedo, M.; Gonzalez Sanchez, H. M.; Castillo, C. G., Astrocytes derived from neural progenitor cells are susceptible to Zika virus infection. *PLoS One* **2023**, 18, (3), e0283429.
27. Veilleux, C.; Eugenin, E. A., Mechanisms of Zika astrocyte infection and neuronal toxicity. *NeuroImmune Pharm Ther* **2023**, 2, (1), 5-18.
28. Miner, J. J.; Cao, B.; Govero, J.; Smith, A. M.; Fernandez, E.; Cabrera, O. H.; Garber, C.; Noll, M.; Klein, R. S.; Noguchi, K. K.; Mysorekar, I. U.; Diamond, M. S., Zika Virus Infection during Pregnancy in Mice Causes Placental Damage and Fetal Demise. *Cell* **2016**, 165, (5), 1081-1091.
29. Cowell, E.; Kris, L. P.; Bracho-Granado, G.; Jaber, H.; Smith, J. R.; Carr, J. M., Zika virus infection of retinal cells and the developing mouse eye induces host responses that contrasts to the brain and dengue virus infection. *J Neurovirol* **2023**, 29, (2), 187-202.
30. Li, Y.; Shi, S.; Xia, F.; Shan, C.; Ha, Y.; Zou, J.; Adam, A.; Zhang, M.; Wang, T.; Liu, H.; Shi, P. Y.; Zhang, W., Zika virus induces neuronal and vascular degeneration in developing mouse retina. *Acta Neuropathol Commun* **2021**, 9, (1), 97.
31. van den Pol, A. N.; Mao, G.; Yang, Y.; Ornaghi, S.; Davis, J. N., Zika Virus Targeting in the Developing Brain. *J Neurosci* **2017**, 37, (8), 2161-2175.
32. Nem de Oliveira Souza, I.; Frost, P. S.; Franca, J. V.; Nascimento-Viana, J. B.; Neris, R. L. S.; Freitas, L.; Pinheiro, D.; Nogueira, C. O.; Neves, G.; Chimelli, L.; De Felice, F. G.; Cavalheiro, E. A.; Ferreira, S. T.; Assuncao-Miranda, I.; Figueiredo, C. P.; Da Poian, A. T.; Clarke, J. R., Acute and chronic neurological consequences of early-life Zika virus infection in mice. *Science translational medicine* **2018**, 10, (444).
33. Snyder-Keller, A.; Bolivar, V. J.; Zink, S.; Kramer, L. D., Brain Iron Accumulation and the Formation of Calcifications After Developmental Zika Virus Infection. *J Neuropathol Exp Neurol* **2020**, 79, (7), 767-776.
34. Snyder-Keller, A.; Kramer, L. D.; Zink, S.; Bolivar, V. J., Mouse Strain and Sex-Dependent Differences in Long-term Behavioral Abnormalities and Neuropathologies after Developmental Zika Infection. *J Neurosci* **2019**, 39, (27), 5393-5403.
35. Ireland, D. D. C.; Manangeeswaran, M.; Lewkowicz, A. P.; Engel, K.; Clark, S. M.; Laniyan, A.; Sykes, J.; Lee, H. N.; McWilliams, I. L.; Kelley-Baker, L.; Tonelli, L. H.; Verthelyi, D., Long-term persistence of infectious Zika virus: Inflammation and behavioral sequela in mice. *PLoS Pathog* **2020**, 16, (12), e1008689.
36. Clancy, B.; Darlington, R. B.; Finlay, B. L., Translating developmental time across mammalian species. *Neuroscience* **2001**, 105, (1), 7-17.
37. Semple, B. D.; Blomgren, K.; Gimlin, K.; Ferriero, D. M.; Noble-Haeusslein, L. J., Brain development in rodents and humans: Identifying benchmarks of maturation and vulnerability to injury across species. *Prog Neurobiol* **2013**, 106-107, 1-16.
38. Metscher, B. D., MicroCT for comparative morphology: simple staining methods allow high-contrast 3D imaging of diverse non-mineralized animal tissues. *BMC Physiol* **2009**, 9, 11.
39. Gignac, P. M.; Kley, N. J., Iodine-enhanced micro-CT imaging: methodological refinements for the study of the soft-tissue anatomy of post-embryonic vertebrates. *J Exp Zool B Mol Dev Evol* **2014**, 322, (3), 166-76.
40. Camilieri-Asch, V.; Shaw, J. A.; Mehnert, A.; Yopak, K. E.; Partridge, J. C.; Collin, S. P., diceCT: A Valuable Technique to Study the Nervous System of Fish. *eNeuro* **2020**, 7, (4).
41. Nasrullah, Q.; Renfree, M. B.; Evans, A. R., Three-dimensional mammalian tooth development using diceCT. *Arch Oral Biol* **2018**, 85, 183-191.
42. Callahan, S.; Crowe-Riddell, J. M.; Nagesan, R. S.; Gray, J. A.; Davis Rabosky, A. R., A guide for optimal iodine staining and high-throughput diceCT scanning in snakes. *Ecol Evol* **2021**, 11, (17), 11587-11603.
43. Gray, J. A.; Gignac, P. M.; Stanley, E. L., The first full body diffusible iodine-based contrast-enhanced computed tomography dataset and teaching materials for a member of the Testudines. *Anat Rec (Hoboken)* **2024**, 307, (3), 535-548.
44. Smith, T. D.; Corbin, H. M.; King, S. E. E.; Bhatnagar, K. P.; DeLeon, V. B., A comparison of diceCT and histology for determination of nasal epithelial type. *PeerJ* **2021**, 9, e12261.

45. Yoakum, C.; Terhune, C., The inferior alveolar nerve and its relationship to the mandibular canal. *Anat Rec (Hoboken)* **2024**, 307, (1), 97-117.
46. Feldman, K. M.; O'Keefe, Y. A.; Gignac, P. M.; O'Brien, H. D., Highest resolution microCT scan of the human brainstem reveals putative anatomical basis for infrequency of medial medullary syndrome. *Neuroimage Clin* **2022**, 36, 103272.
47. Gignac, P. M.; O'Brien, H. D.; Sanchez, J.; Vazquez-Sanroman, D., Multiscale imaging of the rat brain using an integrated diceCT and histology workflow. *Brain Struct Funct* **2021**, 226, (7), 2153-2168.
48. Klaunberg, B. A.; Lizak, M. J., Considerations for setting up a small-animal imaging facility. *Lab Animal* **2004**, 33, (3), 28-34.
49. Szulc, K. U.; Lerch, J. P.; Nieman, B. J.; Bartelle, B. B.; Friedel, M.; Suero-Abreu, G. A.; Watson, C.; Joyner, A. L.; Turnbull, D. H., 4D MEMRI atlas of neonatal FVB/N mouse brain development. *Neuroimage* **2015**, 118, 49-62.
50. Cabezas, S.; Bracho, G.; Aloia, A. L.; Adamson, P. J.; Bonder, C. S.; Smith, J. R.; Gordon, D. L.; Carr, J. M., Dengue Virus Induces Increased Activity of the Complement Alternative Pathway in Infected Cells. *J Virol* **2018**, 92, (14).
51. Dawood, Y.; Hagoort, J.; Siadari, B. A.; Ruijter, J. M.; Gunst, Q. D.; Lobe, N. H. J.; Strijkers, G. J.; de Bakker, B. S.; van den Hoff, M. J. B., Reducing soft-tissue shrinkage artefacts caused by staining with Lugol's solution. *Sci Rep* **2021**, 11, (1), 19781.
52. Thompson, C. L.; Ng, L.; Menon, V.; Martinez, S.; Lee, C. K.; Glattfelder, K.; Sunkin, S. M.; Henry, A.; Lau, C.; Dang, C.; Garcia-Lopez, R.; Martinez-Ferre, A.; Pombero, A.; Rubenstein, J. L. R.; Wakeman, W. B.; Hohmann, J.; Dee, N.; Sodt, A. J.; Young, R.; Smith, K.; Nguyen, T. N.; Kidney, J.; Kuan, L.; Jeromin, A.; Kaykas, A.; Miller, J.; Page, D.; Orta, G.; Bernard, A.; Riley, Z.; Smith, S.; Wohnoutka, P.; Hawrylycz, M. J.; Puelles, L.; Jones, A. R., A high-resolution spatiotemporal atlas of gene expression of the developing mouse brain. *Neuron* **2014**, 83, (2), 309-323.
53. Fedorov, A.; Beichel, R.; Kalpathy-Cramer, J.; Finet, J.; Fillion-Robin, J. C.; Pujol, S.; Bauer, C.; Jennings, D.; Fennessy, F.; Sonka, M.; Buatti, J.; Aylward, S.; Miller, J. V.; Pieper, S.; Kikinis, R., 3D Slicer as an image computing platform for the Quantitative Imaging Network. *Magn Reson Imaging* **2012**, 30, (9), 1323-41.
54. Rolfe, S.; Pieper, S.; Porto, A.; Diamond, K.; Winchester, J.; Shan, S.; Kirveslahti, H.; Boyer, D.; Summers, A.; Maga, A. M., SlicerMorph: An open and extensible platform to retrieve, visualize and analyse 3D morphology. *Methods Ecol Evol* **2021**, 12, (10), 1816-1825.
55. Cignoni, P.; Corsini, M.; Ranzuglia, G., MeshLab: an Open-Source 3D Mesh Processing System. *Ercim News* **2008**, (73), 45-46.
56. Kazhdan, M.; Hoppe, H., Screened Poisson Surface Reconstruction. *Acm T Graphic* **2013**, 32, (3).
57. Team, R. c. R: A language and environment for statistical computing. URL <https://www.R-project.org/>
58. Gignac, P. M.; Kley, N. J.; Clarke, J. A.; Colbert, M. W.; Morhardt, A. C.; Cerio, D.; Cost, I. N.; Cox, P. G.; Daza, J. D.; Early, C. M.; Echols, M. S.; Henkelman, R. M.; Herdina, A. N.; Holliday, C. M.; Li, Z.; Mahlow, K.; Merchant, S.; Muller, J.; Orsbon, C. P.; Paluh, D. J.; Thies, M. L.; Tsai, H. P.; Witmer, L. M., Diffusible iodine-based contrast-enhanced computed tomography (diceCT): an emerging tool for rapid, high-resolution, 3-D imaging of metazoan soft tissues. *J Anat* **2016**, 228, (6), 889-909.
59. Wurm, J.; Konttinen, H.; Andressen, C.; Malm, T.; Spittau, B., Microglia Development and Maturation and Its Implications for Induction of Microglia-Like Cells from Human iPSCs. *Int J Mol Sci* **2021**, 22, (6).
60. Chen, V. S.; Morrison, J. P.; Southwell, M. F.; Foley, J. F.; Bolon, B.; Elmore, S. A., Histology Atlas of the Developing Prenatal and Postnatal Mouse Central Nervous System, with Emphasis on Prenatal Days E7.5 to E18.5. *Toxicol Pathol* **2017**, 45, (6), 705-744.
61. Sequerra, E. B.; Rocha, A. J.; de Medeiros, G. O. C.; Neto, M. M.; Maia, C. R. S.; Arrais, N. M. R.; Bezerra, M.; Jeronimo, S. M. B.; Barros, A. K.; Sousa, P. S.; Nogueira de Melo, A.; Queiroz, C. M., Association between brain morphology and electrophysiological features in Congenital Zika Virus Syndrome: A cross-sectional, observational study. *EClinicalMedicine* **2020**, 26, 100508.
62. Harding, A. T.; Ocwieja, K.; Jeong, M.; Zhang, Y.; Leger, V.; Jhala, N.; Stankovic, K. M.; Gehrke, L., Human otic progenitor cell models of congenital hearing loss reveal potential pathophysiologic mechanisms of Zika virus and cytomegalovirus infections. *mBio* **2024**, 15, (4), e0019924.
63. Ginhoux, F.; Lim, S.; Hoefel, G.; Low, D.; Huber, T., Origin and differentiation of microglia. *Front Cell Neurosci* **2013**, 7, 45.
64. Hattori, Y., The multifaceted roles of embryonic microglia in the developing brain. *Front Cell Neurosci* **2023**, 17, 988952.
65. Mehl, L. C.; Manjally, A. V.; Bouadi, O.; Gibson, E. M.; Tay, T. L., Microglia in brain development and regeneration. *Development* **2022**, 149, (8).
66. Wen, W.; Cheng, J.; Tang, Y., Brain perivascular macrophages: current understanding and future prospects. *Brain* **2024**, 147, (1), 39-55.

67. Linsley, J. W.; Reisine, T.; Finkbeiner, S., Three dimensional and four dimensional live imaging to study mechanisms of progressive neurodegeneration. *J Biol Chem* **2024**, 300, (7), 107433.
68. Rolfe, S. M.; Whikehart, S. M.; Maga, A. M., Deep learning enabled multi-organ segmentation of mouse embryos. *Biol Open* **2023**, 12, (2).

**Disclaimer/Publisher's Note:** The statements, opinions and data contained in all publications are solely those of the individual author(s) and contributor(s) and not of MDPI and/or the editor(s). MDPI and/or the editor(s) disclaim responsibility for any injury to people or property resulting from any ideas, methods, instructions or products referred to in the content.